Fatigue behavior of 17-4 PH parts produced by Material Extrusion Additive Manufacturing: A study on thickness and notch effects

Saveria Spiller
Norwegian University of Science and Technology, Trondheim, Norway
(Current address: University of Padova, Italy)
saveria.spiller@unipd.it https://orcid.org/0009-0007-5924-4623

Armin Habibiyan
Norwegian University of Science and Technology, Trondheim, Norway
(Current address: Katholieke Universiteit Leuven, Belgium)
armin.habibiyan@kuleuven.be, https://orcid.org/0009-0008-3242-5093

Ole-Bjørn Ellingsen Moe
Mechatronics Innovation Lab, Grimstad, Norway
Ole-Bjorn@mil-as.no

Sara Bagherifard
Politecnico di Milano, Milan, Italy
sara.bagherifard@polimi.it https://orcid.org/0000-0002-5757-2785

Nima Razavi
Norwegian University of Science and Technology, Trondheim, Norway
nima.razavi@ntnu.no https://orcid.org/0000-0002-2574-065X

ABSTRACT. 17-4 PH specimens were produced using the three-step process referred to as Material Extrusion Additive Manufacturing (MEAM), which involves printing components with a composite feedstock of metal powder and polymers, followed by a debinding process to remove the polymer, and a final sintering process to obtain the finished metallic part. The process enables the production of metallic components at a limited cost and with reduced safety issues in comparison to other additive manufacturing processes. With the goal of exploring and evaluating the fatigue properties of 17-4 PH MEAM

Citation: Spiller, S., Habibiyan, A., Ellingsen Moe, O., Bagherifard, S., Razavi, N., Fatigue behavior of 17-4 PH parts produced by Material Extrusion Additive Manufacturing: A study on thickness and notch effects, 77 (2026) 386-404.

Received: 28.04.2026
Accepted: 04.06.2026
Published: 13.06.2026
Issue: 07.2026

specimens, two experimental campaigns were designed. The first with the objective of assessing the effect of thickness on the fatigue performance of smooth specimens, and the second aimed to investigate the notch effect on the fatigue limit of different notched specimens. The smooth specimens were fabricated with a thickness ranging between 1 and 5 mm, while the notched specimens were fabricated with a thickness of 3 mm, with 90° and 30° notch opening angles. The mechanical properties of the smooth series proved not to be affected by the thickness, neither for quasi-static nor cyclic response. On the contrary, the fatigue behavior of the notched specimens was significantly influenced by the presence of the notch, with sharper notches exhibiting a more negative impact. Moreover, the findings revealed that the fabrication of specimens characterized with thin sections, small geometrical features, and acute notches presented significant challenges, posing a severe issue regarding the practical applicability of MEAM for real-life complex geometries.

KEYWORDS. Additive, Stainless steel, Fatigue, Thickness, Notch.

INTRODUCTION

Material Extrusion Additive Manufacturing (MEAM) is a multiphase process that allows the production of metallic parts starting from a feedstock composed of metal powder dispersed in a polymeric matrix. The process involves the following steps: printing of the so-called green parts, an intermediate product, i.e., the metal powder dispersed in a polymeric matrix; debinding, which is a thermal or chemical process needed to remove the polymeric binder from the green part; and sintering, a well-known metallurgical process that enables metal powder diffusion to obtain a dense metallic part, called the silver part. The potential of MEAM, thoroughly discussed in several reviews and studies [1-4], is mainly related to its beamless fabrication process and inexpensiveness when compared to other metal AM processes. However, some fabrication issues remain unsolved, hindering the wide diffusion of this manufacturing technique.

The feedstock, often called Highly-filled Polymer (HP), can be found in different shapes, such as rods or pellets, but it is usually provided in the shape of a filament [5]. Indeed, commercial Fused Deposition Modeling (FDM) printers designed to extrude polymeric filaments to produce three-dimensional parts are potentially appropriate to be used with HP filament, too. These printers are, in general, affordable, easy to operate, and do not pose any peculiar safety issues. The idea of using such an apparatus to print composite parts that can be further processed to obtain metallic components is understandably attractive. However, these systems are not designed to guarantee high-quality standards, robustness, and accuracy, which might be unacceptable depending on the final use of the fabricated components. Nowadays, the interest in the MEAM process has pushed the development of commercial systems specifically designed to deal with the HP feedstock, which includes the required hardware for each stage of the process. One of the most widely used MEAM systems is the Metal X platform, developed by Markforged. Metal X has been employed for the fabrication of the specimens investigated in the present research.

The feasibility of the process and the quasi-static properties of 17-4 PH specimens fabricated with the Metal X system have been evaluated in different studies available in the literature. Galati et al. [6] fabricated and studied 17-4 PH samples with different infill strategies, reporting high manufacturing precision, although the density and residual porosity of the parts were not satisfactory. Nonetheless, the authors mentioned that high density was not required for the considered applications, including jaws or jigs in machining and welding operations. Henry et al. [7] performed a similar study with a focus on the effect of the building orientation on the quasi-static mechanical properties of the MEAM parts; They reported that the maximum tensile strength was reached for specimens printed flat on the platform, while the specimens printed with a 'vertical' layout were weaker and characterized by very limited elongation to fracture. Other works on the anisotropy of MEAM parts' tensile properties can be found in [8-10], reporting similar outcomes. In conclusion, Metal X proves to be a reliable process when it comes to tensile properties, guaranteeing an Ultimate Tensile Strength (UTS) around 1000 MPa and elongation to fracture below 6% [7, 11-13] when the tensile specimens are printed in a favorable orientation. Similar performances might not be reached when less established routes are followed, involving the in-house production of the filament or the use of a generic FDM printer available on the market. An example of a similar fabrication route is provided in [14]: although the authors attempted different configurations of printing parameters, the maximum UTS reached was 792 MPa, significantly below the standard UTS of 17-4 PH parts in both solution-treated and aged conditions, as per the ASTM standard A693-24 [15]. Indeed, aging treatments improve the performance of wrought 17-4 PH, thus Pellegrini et al. [16] compared the efficiency of two standard heat treatments (H900 and H1050) on MEAM parts produced through two commercial MEAM systems (Desktop Metals and Metal X) to reduce porosity and increase microhardness. The response of MEAM parts to the heat treatments was reported to be positive and comparable to that of hot-rolled 17-4 PH. Similarly, Gong et al. [17] performed the H900 treatment on notched specimens that were tested in situ inside an SEM chamber to investigate the deformation mechanisms, also proving that the heat treatment improved the parts' homogeneity, although it did not alter the fracture mechanisms observed.

Limited research has been conducted so far about the fatigue behavior of 17-4 PH MEAM specimens, implying a significant knowledge gap worsened by the intrinsically complicated nature of the fatigue behavior of a metal material. Axial fatigue tests on specimens with circular cross-sections were performed in [11]: the study focused on the comparison between MEAM specimens fabricated with different densities and wrought counterparts. The wrought specimens showed a fatigue limit at around 40% of their UTS, while the full-density MEAM parts gave a much lower fatigue behavior, with an expected fatigue limit below 20% of their UTS. The poor fatigue behavior of the MEAM parts was attributed to the abundant internal defects; however, it might be sufficient and appropriate for low-cycle fatigue applications. Kedziora et al. [18] proposed a wide comparison between additive manufacturing techniques, including axial fatigue testing of 17-4 PH Metal X specimens that were printed vertically on the printing platform. As for the tensile properties, the unfavorable building orientation proved to be detrimental to the fatigue limit. The vertical specimens indeed performed poorly and showed a fracture surface with signs of delamination, suggesting very poor adhesion between layers. The inadequacy of the vertical layout was further proved in [19], an investigation on ultra-high cycle fatigue, and in [12]. To conclude, some research focused on the improvement of the fatigue behavior of 17-4 PH MEAM parts through the alteration of the specimens' surface. Rodriguez et al. [12] showed that MEAM 17-4 PH specimens machined in a lathe to remove the outer surfaces performed better than their counterparts in as-sintered conditions. Shot peening was also proven to be very effective in improving the fatigue life of MEAM 17-4 PH specimens [20], with a much more relevant impact than thermal processes.

The Markforged system and the 17-4 PH filament by the same brand were used to produce the specimens tested in the present work. Non-mechanical and mechanical test campaigns were planned to evaluate the quality of the as-printed and as-sintered specimens, focusing on their fatigue properties. Fatigue behavior depends on multiple factors, and it is not always appropriate to refer to the fatigue behavior of a material as a material property. Fatigue investigations are carried out with specimens that are often designed following standards or best practices; in contrast, real-world components do not always present a regular shape. Geometrical irregularities, section variations, and notches can drastically decrease the resistance of a part from what is observed in a laboratory. Thus, in the present study, it was deemed relevant to increase the degree of reality of the tests by varying the design of the specimens. In particular, the research revolves around two issues that, to the best of the authors' knowledge, have not yet been investigated for MEAM technology. The first is the thickness effect. Fatigue specimens were printed with the same design but different thicknesses to evaluate how the number of layers in a part can affect its properties. Second, notched parts were printed, with different notch geometries, to evaluate the notch effect on the fatigue properties of the MEAM 17-4 PH specimens.

The paper is organized as follows: the next section, Section 2, Materials and Methods, describes the fabrication process and the test equipment, as well as the procedures adopted to characterize the specimens. In Section 3, Results and Discussion, the characterization of the green and silver parts is presented, with a dedicated sub-section to fatigue properties, including thickness effect, notch effect, and fractography analysis. Finally, Section 4, Conclusions, summarizes the main outcomes of the research and provides some useful recommendations.

MATERIAL AND METHODS

Specimen fabrication

The system by Markforged is equipped for every stage of the process: the printer, named Metal X, the washing system Wash-1, and the sintering furnace Sinter-2. The printer has a dual-nozzle printing head that allows the deposition of different materials in the same print. Indeed, a ceramic compound can be used in the interfaces between parts and supports to ease their removal since the layer of ceramic, with different thermal properties, remains in a powdery state, making the interface with the supports easy to break. The system proposes a set of optimized parameters for each step of the process; hence, a limited number of choices can be made by the user. This is simultaneously a drawback and a benefit, depending on the purpose of the users.

17-4 PH fatigue specimens were fabricated with the dimensions reported in Fig. 1. The specimens were printed flat on the printing platform, meaning that the building direction was parallel to their thickness. The infill strategy adopted consisted of full-density rectilinear rasters with +45°/-45° inclination. Four contour walls were printed around the infill. The specimens were printed without any brim or raft. The specimens' shrinkage was compensated automatically by the software associated with Metal X, the Markforged Eiger software. The experimental plan involved the fabrication of five types of fatigue specimens, divided into two categories: the smooth and the notched series. The smooth specimens were characterized by rounded sides and a rectangular cross-section, giving a stress concentration factor of 1.07 based on net section stresses. Three batches with thicknesses of $t=1$, 3, and 5 mm were fabricated. The notched specimens were fabricated with a 3 mm thickness and two V-notch geometries with opening angles of $2\alpha=30^\circ$ and $2\alpha=90^\circ$, respectively. The design also entailed different notch radii ϱ; $\varrho=0$ mm for the narrow notch, and $\varrho=1$ mm for the wider notch.

The nomenclature that is adopted from now on is the following: S1, S3, and S5 indicate smooth specimens with $t=1$ mm, $t=3$ mm, and $t=5$ mm. N30 indicates the notched specimens with $2\alpha=30^\circ$ and notch radius 0 mm, while N90 indicates the specimens with $2\alpha=90^\circ$ and notch radius 1 mm. Each specimen per batch is also referred to with a progressive number to distinguish them (e.g., S3-1 indicates the first specimen of the smooth batch with 3 mm thickness), although no differences were expected between specimens belonging to the same batch.

After the printing phase, the specimens were moved to the second stage of the process, i.e., washing, where the green parts were transformed into another intermediate product, referred to as brown parts. In this stage, the binder is removed through solvent debinding, as required by the Markforged 17-4 PH filament. A washing fluid such as the commercial Opteon Sion was used, and the dwell time was adjusted based on the specimen volume. The process is deemed completed once a target value of weight loss is met, which means that a sufficient share of the binder has been removed. After washing, the specimens were moved to the sintering furnace. A first temperature step was applied to remove the remaining binder components, and then a longer step at 1100°C was considered to complete the densification. A reducing atmosphere in the furnace was obtained with a mixture of A_2 and H_2.

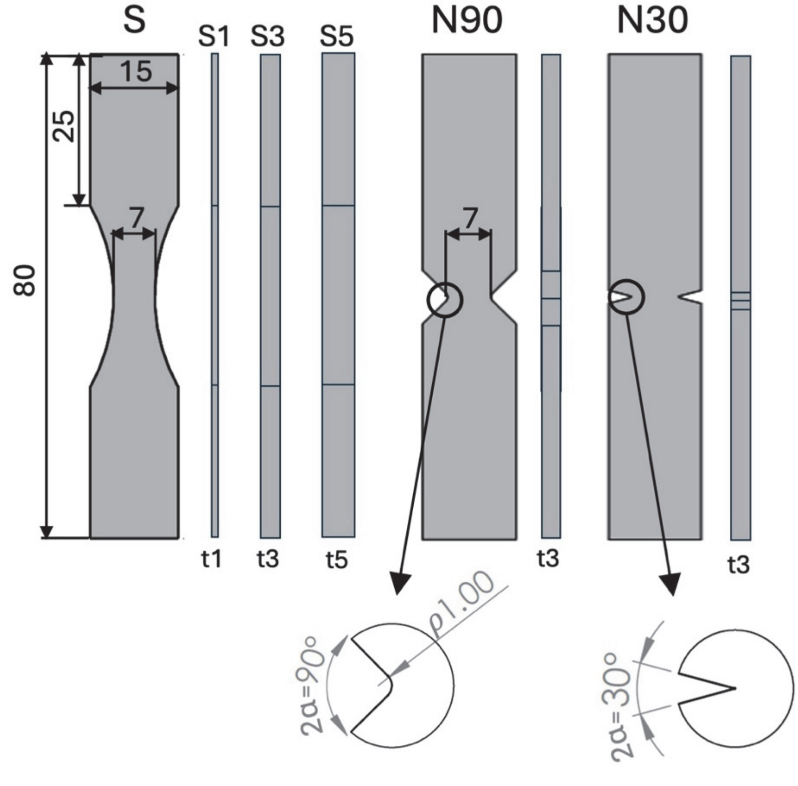

Figure 1: Design of the specimens and nomenclature. All the dimensions are in mm.

Non-mechanical analysis

Green parts and silver parts were examined before starting the mechanical characterization campaign to evaluate the quality of the fabrication process. An optical investigation was carried out with the optical microscope Hirox rH2000, and the specimens' dimensions were measured with a digital caliper. Tensile tests were also carried out on the green parts, with the sole purpose of revealing the fracture surfaces obtained. The shrinkage of the specimens, a natural consequence of the debinding and sintering process, was assessed through the calculation of the linear reduction *LR%* of the specimens' main dimensions (thickness, total length, and maximum width) as $LR\%=100\times(d_g-d_s)/d_g$, where d_g is the green parts dimensions and d_s is the sintered parts dimensions. The density of the silver parts was measured with the Archimedean method, which requires the weight of the specimens in air, m_a, and in water, m_w, to combine the values as $p=m_a/(m_a-m_w)$. The surface roughness was measured using the confocal microscope ALICONA Infinite Focus SL G4 (IFM). Finally, the microstructure and the porosity content were evaluated on the cross-sections of the smooth specimens. The cross-sections were prepared following a classic metallographic preparation, and the Vilella reagent (1 g picric acid, 5 ml HCl, and 100 ml ethanol) was used to reveal the microstructure.

Mechanical tests and fractography

The thickness effect was evaluated through several mechanical tests. First, Vickers microhardness tests were conducted using the Mitutoyo MicroWidZhard HM-200 series apparatus with a diamond indenter and an indentation load of 0.2 kgf. Cross-sectional microhardness measures were repeated on one smooth specimen for each thickness. The indentations were distributed along three parallel lines from the outer surface towards the core to evaluate possible hardness variations in each specimen's bulk.

Smooth specimens were also tested under tensile loading conditions to evaluate their tensile properties and the possible influence of their thickness. This also allowed the comparison of the MEAM specimens with conventional material, and the correlation of their corresponding UTS to the fatigue properties evaluated. The tests were conducted with the MTS Landmark 370 equipped with a 50 kN load cell, in displacement control with a displacement rate of 1 mm/min. The engineering strain was computed with the DIC technique, which implies the use of an image recording apparatus and the painting of the specimens with a suitable speckle pattern. The painting was done with black and white spray cans of paint to achieve a black speckled pattern on a homogeneous white background. The size and dispersion of the speckle affect the accuracy of the analysis; a tradeoff between the readability and density of the black speckle was made. The camera used is an Allied Vision Stingray F-504B with a resolution of 5 Mpx. The images recorded were processed in the commercial software Vic 2D, able to correlate the deformation of the speckle pattern in each image with respect to the reference image representing the initial moment of the test.

The same testing machine was used to perform uniaxial fatigue tests. Both the specimen categories were tested to evaluate the thickness effect and the notch effect. The test frequency was set to 20 Hz, the ratio of the cyclic load was $R=\sigma_{min}/\sigma_{max}=0.1$, and the specimens were considered run-out when exceeding 2×10^6 cycles. The fracture surfaces of broken specimens were then analyzed using the SEM FEI-QUANTA 650 FEG and the confocal microscope.

RESULTS AND DISCUSSION

Green part analysis

The study on the green parts involved three specimens: S3 (smooth with t=3 mm), N30 (notched with $2\alpha=30°$ and $\varrho=0$ mm), and N90 (notched with $2\alpha=90°$ and $\varrho=1$ mm). Fig. 2 shows distinctive features of the green parts observed with the optical microscope from different perspectives. The specimens were also fractured using a tensile test machine to observe their infill. The average layer thickness was calculated as 0.16 ± 0.02 mm. The four contour walls are clearly visible in Figs. 2e-f, thanks to the peculiar porosity pattern that will be commented on later. However, it must be noted that from the sole observation of Fig. 2a, only three contour walls are visible due to the overlap of the infill and contour. Regarding the notches, the opening angles were 32° and 92°, respectively, and the corresponding notch radii were measured to be 0.1 and 0.96 mm. This suggests an adequate accuracy achieved during the printing phase. The strength of the green part was estimated through the tensile tests, with a maximum strength achieved of 10 MPa for the smooth part and 1.3 MPa for the notched parts. The strength of the smooth specimen is in good accordance with what was obtained in [21], where a thorough optimization of the printing parameters was carried out to improve the properties of the green parts. The fracture surfaces (Figs. 2e and f) showed a very homogeneous and dense infill, while four arrays of voids were visible on each side, representing the boundaries between the four external walls.

Silver parts analysis

The optical investigation performed on the silver parts revealed a very good dimensional accuracy of all the studied specimens, except for the notch radius of the notched series. The average notch radius obtained for specimens N30, ideally designed with $\varrho=0$, was measured as 0.1 ± 0.02 mm, while for the specimen N90, which should have a blunt notch with $\varrho=1$

mm, it was 0.21±0.06 mm. These values prove that the ideal sharp notch with ϱ=0 mm can not be fabricated and that the sintering process tends to make the notches sharper.

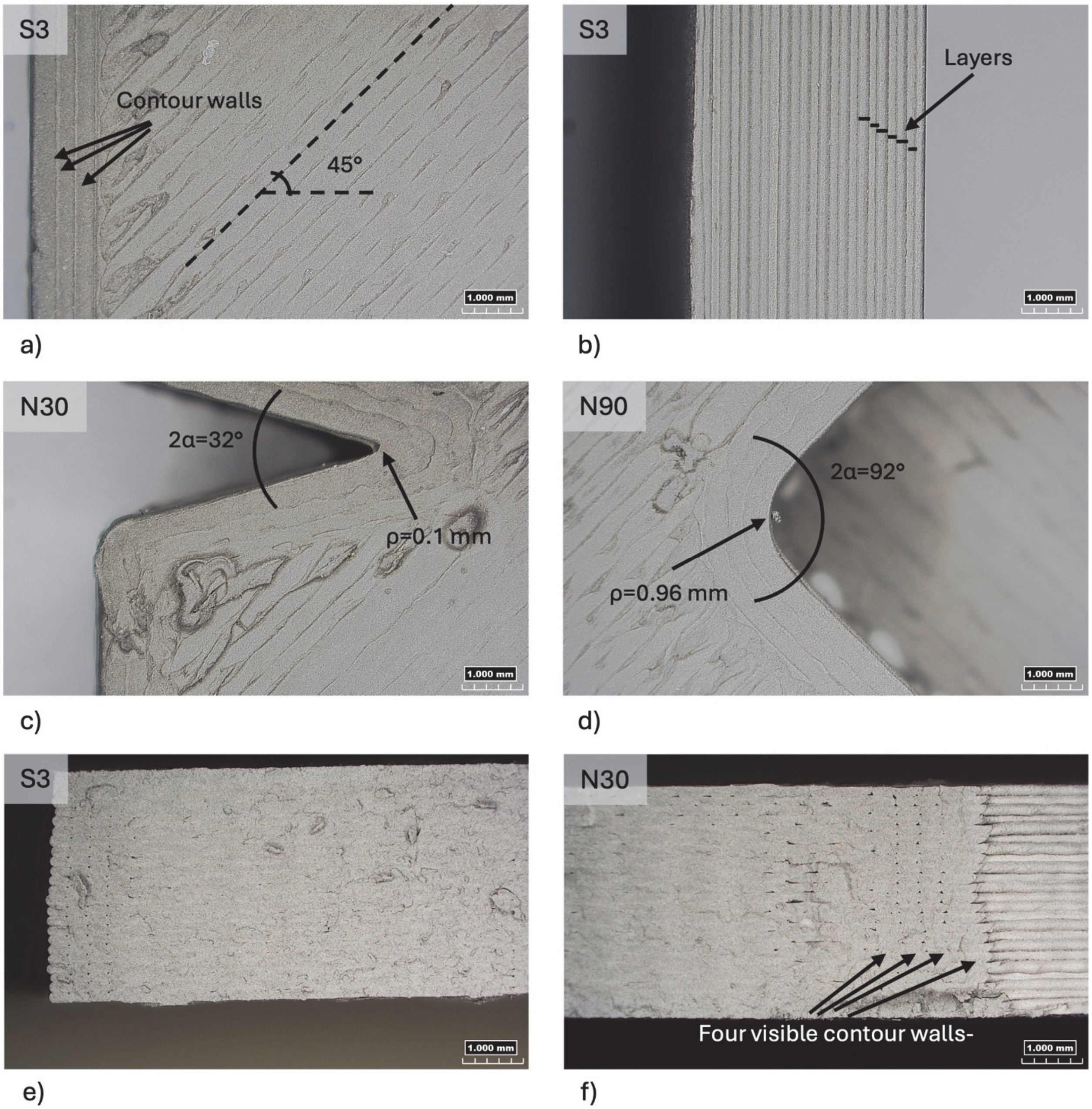

Figure 2: Representative images of the green part S3 top surface (a), and lateral surface (b); comparison of the two notch geometries investigated, N30 (c), and N90 (d); fracture surface of the S3 (e), and notched specimen N30 (f).

According to the producers, the corrective factors that the Metal X system uses to increase the dimensions of the parts on the STL files to compensate for the shrinkage are 1.18 for the dimensions on the x-y plane, which is the printing platform plane, and 1.20 for the z direction, corresponding to the thickness of the parts. This means that the overdimensioning factors are +18% and +20%, respectively. According to the calculations, the linear reduction of the dimensions on the x-y plane between silver and green parts is on average 15%. The linear reduction of the z-direction is highly influenced by the thickness itself. Fig. 3a shows the increasing trend of the linear reduction with increasing specimen thickness. This could be explained by considering that the shrinkage is related to the thinning of the binder pools at layer interfaces [22]. Thus, such a reduction could be directly correlated to the number of layers, which is higher in thick specimens.

Due to the large shrinkage variations correlated to the thickness, the deviation of the silver parts' thicknesses from the target dimensions increased with decreasing thickness, as shown in Fig. 3b. This error was calculated as $error\%=100\times(d_s-d_t)/d_t$, where *dt* is the target dimension. Apparently, the accuracy of the process increases for larger thicknesses. The trend suggests that above t=5 mm, this error tends to zero.

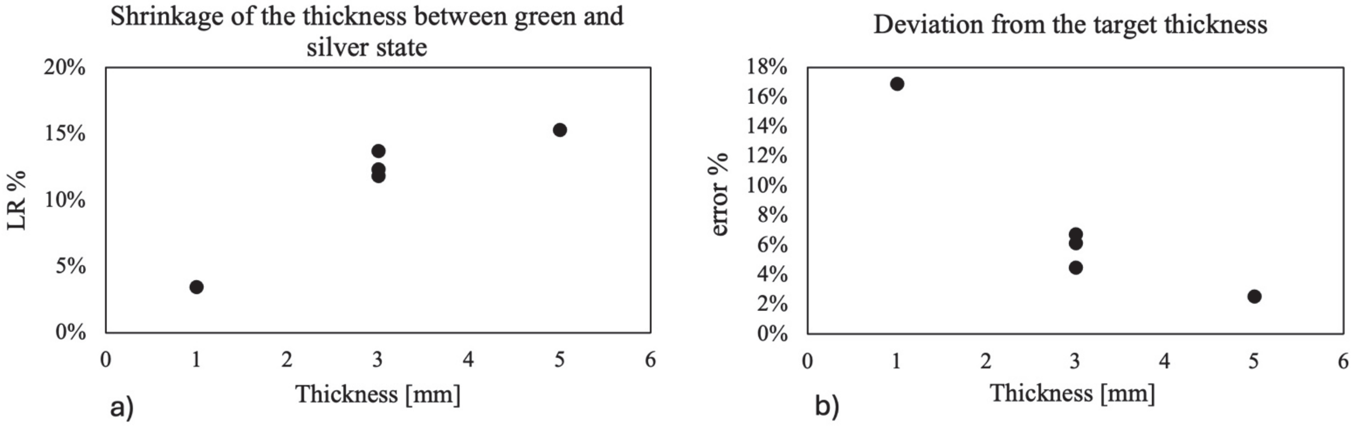

Figure 3: a) variation of the linear reduction between green and silver parts' thickness; b) variation of the relative error between silver parts dimensions and target dimensions in terms of thickness.

The relative density of the parts, measured via Archimedes' method, was calculated as 97% on average, considering 7.75 g/cm^3 as a reference density for 17-4 PH [6]. Similar results were reported in [9-10].

With regards to the surface roughness, the parameter Ra (Arithmetic Average Roughness) was measured on smooth specimens, performing multiple measurements on the top, bottom, and side surfaces. On average, Ra was 6.7±1.6 μm on the top surfaces, 5.3±0.5 μm on the bottom surfaces, and 2.5±0.3 μm on the side surfaces. Due to the constant contact with the platform during the printing and sintering process, the bottom surfaces were expected to be smoother. These values are in line with what was found in other investigations [6, 12, 20].

Fabrication issues

After the thorough evaluation of the green and silver parts, some observations on the quality of the fabrication can be drawn. First of all, it must be underlined that 49 specimens were successfully fabricated and used for the present study. Previous research projects carried out by the same research group involving the use of a commercial FDM printer by Prusa and a commercial HP filament by Ultrafuse BASF [23] let us infer that a production series with this dimension would have been very challenging and time-consuming with such equipment. Metal X proves indeed to be a more robust system, relative to other options available. Moreover, possessing the washing and sintering stations alongside the printer enables optimized fabrication times. However, some defects and issues with the fabrication process must be underlined.

First of all, as reported in Fig. 3, the accuracy of the printer is correlated to the thickness of the parts, suggesting difficulties with printing very thin geometries. The S1 specimens, the thinnest, were indeed challenging to print to the point that the target number of printed specimens was not met due to frequent printing failures; only 9 specimens were fabricated instead of 10. The S1 specimens suffered significantly from warping, exhibiting excessive deformation of the bottom layers.

The density of the specimens was measured through Archimedes' method. Additionally, it was chosen to section and polish one smooth, undeformed specimen per thickness to evaluate the internal porosity distribution. The procedure was repeated on cross-sections at several heights to confirm the continuous nature of the voids in the specimens. For the sake of brevity, Fig. 4 collects only the polished cross-sections cut from the middle of the specimens. It can be observed that the vertical alignment of pores between the contour walls is common to all the thicknesses. This can be explained considering that the external walls were printed at a reduced speed, giving more time for the material to solidify, thus preventing proper adhesion between walls. On the contrary, the infill was relatively homogeneous in both S1 and S5. The same result was obtained in [11], where Computed Tomography (CT) scan analysis proved that the cross-sections were homogeneous and dense in the infill, while wide pores were clearly visible along the four outer perimeters. A peculiar porosity pattern was observed in the S3, which was proven, through further investigations, to affect every single S3 specimen with different intensity. At approximately mid-thickness, a line of expanded pores was visible. This might be related to some unexpected event during the printing phase, such as a possible vibration of the printing platform. This suggests that although the system is more robust than other equipment not conceived to deal with high-filled filaments, the quality of the process is still at stake.

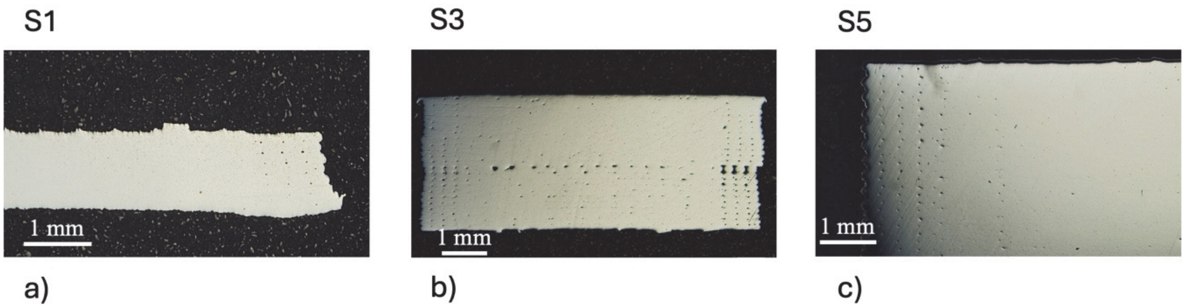

Figure 4: Porosity distribution in the mid-length cross-sections of the smooth specimens at different polishing depths.

Additional observations were made on the notched specimens. Although the green parts were very accurate both in terms of notch opening angle and notch radius, the accuracy of the notch geometries was lost after debinding and sintering phases. Moreover, a very critical defect was observed in all the notches of N30 and some of the N90 specimens, which are cracks starting from the notch root. The average length of the cracks was measured to be 0.27±0.14 mm. The cracks are believed to be sintering cracks, as proved by the SEM investigation. As shown in the magnification of Fig. 5a3, the internal surfaces of the cracks did not show signs of fracture. These surfaces solidified as free surfaces, suggesting that the cracks opened at a very early stage of the sintering process. This issue posed a methodological concern about the significance of the planned experimental campaign. However, due to the explorative nature of the present research, the campaigns were carried out as planned. This also poses a very relevant challenge related to the printing of critical details that go beyond the accuracy achievable during the printing phase.

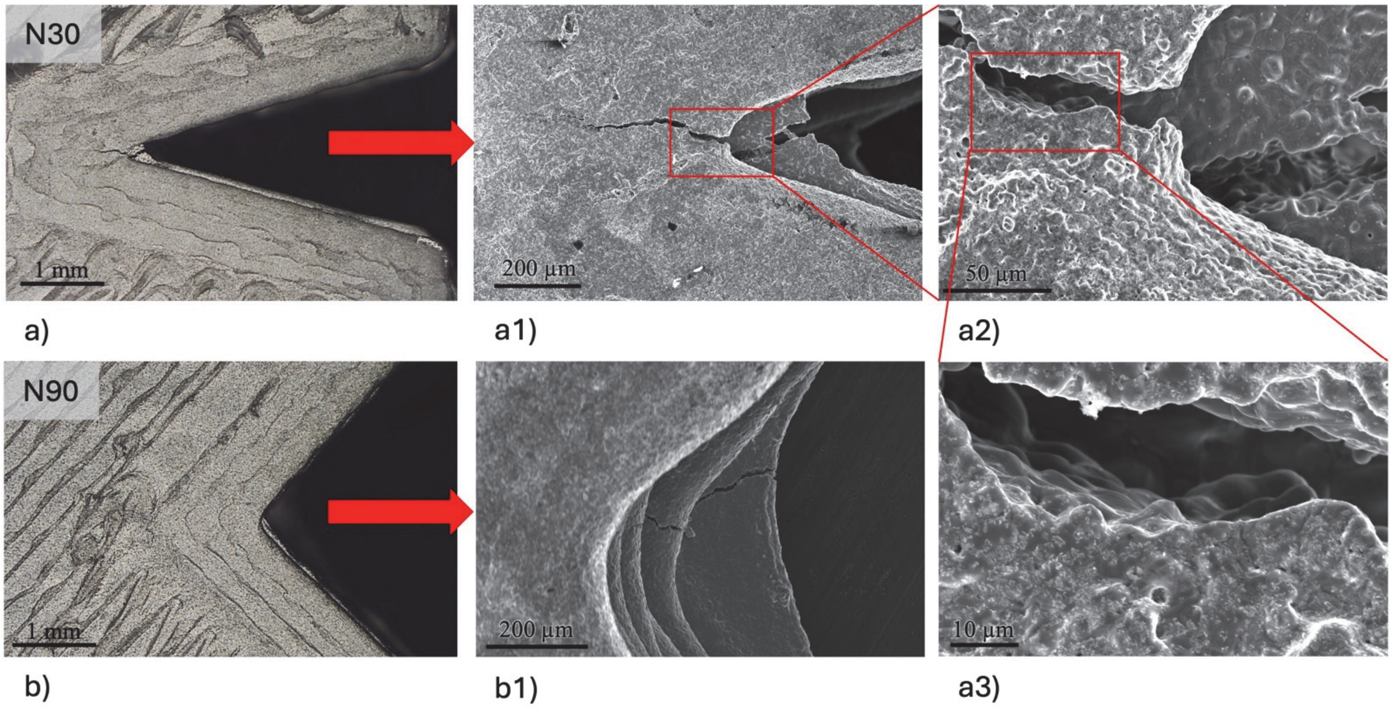

Figure 5: Optical microscope and SEM picture of the notches and magnifications of the sintering cracks. N30 a, a1, a2, a3); N90 b, b1).

Microstructure and microhardness measurements

Fig. 6 shows the plots of the microhardness trend in the cross-sections of the smooth specimens and the typical martensitic microstructure observed close to the surface and in the middle of the etched cross-sections. The microhardness indentation scheme is also reported to help the reading of the plots. The data suggests discrete stability of the microhardness with increasing depth from the upper surface since the values relative to the three lines (depicted with different colors) are similar. This is observed regardless of the thickness of the specimens. Apparently, the microhardness of specimens S3 and S5 tends to increase from the sides to the core of the sections. This variation is unlikely to be related to microstructural features since the sintering process induces a very homogeneous microstructure, as shown in Figs. 6a, b. More likely, the microhardness increase is due to the enhanced density in the core of the specimens, as presented in the previous section.

When comparing the three datasets, the averages obtained suggest a similarity between S1 and S5 (347±8 and 349±8 HV0.2, respectively) and a discrete deviation of S3 (366±8 HV0.2). It must be noted that for this specimen batch, a suitable statistical analysis led to the exclusion of one outlier data point through the Chauvenet criterion, which was performed after the normality of the distribution was confirmed through the χ^2 test. ANOVA one-way analysis was then performed to evaluate the significance of the differences observed between the S1, S3, and S5 batches, with a confidence level of $p=0.05$. The test gave a negative outcome, which means that the datasets shall be considered different, thus suggesting a thickness effect on the microhardness. Nonetheless, the positive result of the Student T-test performed on the sole S1 and S5 datasets proves that they belong to the same statistical population. Thus, it does not seem plausible that higher average microhardness of the intermediate thickness specimens of the S3 series is the result of a thickness effect. Macroscopically, a very peculiar porosity trend was observed in the S3 specimen, as reported in Fig. 4, but the abundance of voids would have had the opposite effect on the hardness, promoting a decrease in it. Thus, considering that the range of thicknesses studied is limited, it is correct to infer that the thickness effect on the microhardness can not be resolved from the results of the present investigation, although nothing suggests a significant impact of it.

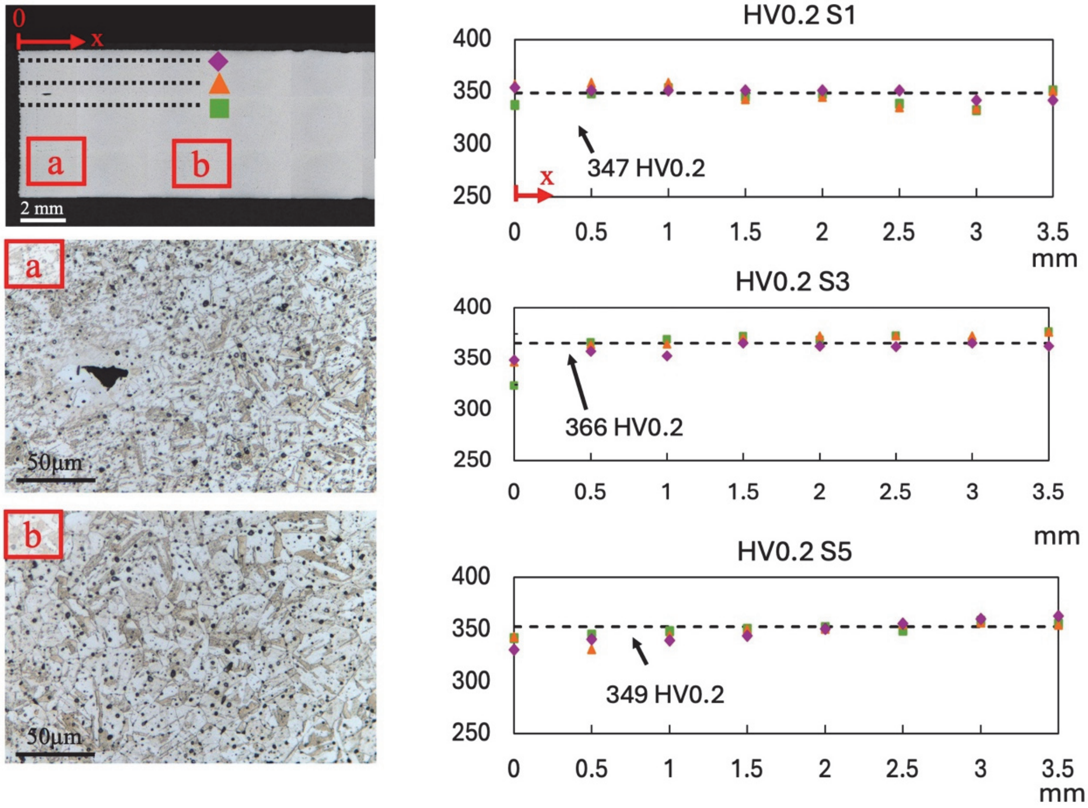

Figure 6: Microstructure and microhardness analysis on the smooth specimens. In the top left corner, a schematic of the indentations shall ease the reading of the plots. The microstructure was also observed in the regions (a) and (b) of the cross-sections. On the right, one plot is dedicated to each thickness.

Tensile tests

The tensile test results are reported in Fig. 7 and Tab. 1. The plot reports the engineering stress-strain curves of the smooth specimens. It must be noted that the design of the specimens is the same as that used for the fatigue tests. The fracture location coincides with the narrow section, which was used to calculate the resistant area in the calculation of the engineering stress. The engineering strain is obtained from the DIC analysis.

As shown by the plot and the table, minor differences can be seen among Young's modulus (E), 0.2% offset yield stress (σ_y), and tensile strength (UTS) of specimens with different thicknesses. The elongation to fracture appeared as the most affected property, showing an increasing trend with increasing thickness. A similar behavior was observed in an investigation on additive manufacturing PBF-EB Ti-6Al-4V specimens reported in [24], where the decrease in the load-bearing capability was associated with decreasing thickness, and the authors explained it based on the grain size and the different impact of the surface features on different thicknesses. The latter explanation fits well with the trend observed in the present work. The irregularities on the MEAM surfaces do not depend on the size of the specimens, as also proven by the surface roughness analysis. These irregularities can act as micro-notches, weakening the specimens. The thinner the section of the specimen, the higher the impact of the micro-notches expected to be, leading to premature failure.

The properties obtained correlate well with the results of other studies in which Metal X was used to fabricate 17-4 PH specimens [7, 11].

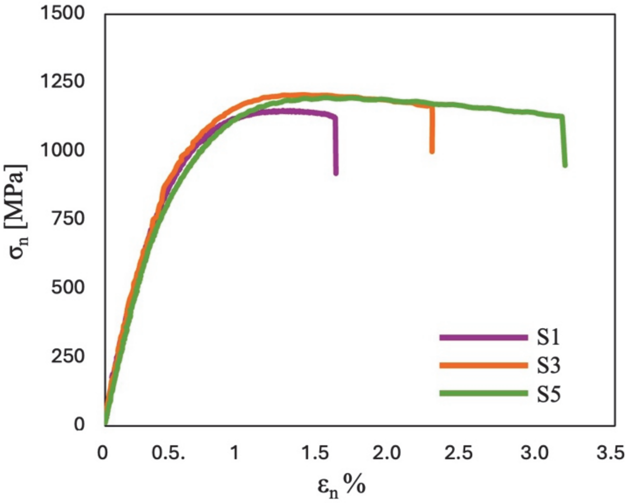

Figure 7: Engineering stress-strain curves obtained with S1, S3, and S5 specimens.

	S1	S3	S5	avg
E [GPa]	211.3	221.2	213.0	215.2±5.3
σ_y [MPa]	1059	1086	1015	1053±36
UTS [MPa]	1150	1209	1197	1185±31
ε_f	1.59 %	2.24%	3.16%	2.33 ±0.79%

Table 1: Tensile properties per thickness and averages.

Fatigue tests

The results of the axial fatigue tests are reported in Tab. A1 in the Appendix and plotted in Figs. 8a-c, where the S-N curves relative to the S1, S3, and S5 batches are expressed in terms of the maximum stress applied (σ_{max}). A statistical analysis was performed based on the standard ISO 12107 [25] to calculate negative inverse slope k, scatter index T_σ, and statistical fatigue limit $\sigma_{max50\%}$ at 2 milion cycles (run-out) obtained from the statistical analysis corresponding to a survival probability (PS) of 50%. The scatter bands related to PS 10% and 90% were calculated with a confidence level of 95%. The statistical elaboration of the three curves suggests major differences related to the thickness of the specimens. First, the width of the scatter bands increased with the thickness. The scatter index T_σ, obtained as $\sigma_{max10\%}/\sigma_{max90\%}$, was used to quantify the width of the scatter bands. The obtained plots show that T_σ increased from 1.26 to 1.64 and finally to 2.85 for the S1, S3, and S5 specimens. This could be the result of a statistical abundance of defects in the larger cross-sections, leading to higher variability of the data. Regarding the negative inverse slope k, the values calculated are 3.05, 5.12, and 3.79 for t=1, 3, and 5 mm, suggesting an enhanced weakness of the S3 specimens, especially on the left side of the S-N curve, towards high load levels. This behavior is unlikely to be related to the thickness of the specimens, but it might be a result of the peculiar porosity pattern reported in Fig. 4 on the S3 batch.

A run-out was obtained for all the thicknesses at a stress level σ_{max}=300 MPa. This suggests, in the first place, that the fatigue life of the specimens at low-stress levels might be independent of the thickness, although further tests on the high-cycle segment of the fatigue curve are required to extrapolate a precise trend. Secondly, the physically derived fatigue limit-obtained from the observation of the S-N curve, which for steel usually present a *knee,* shall be placed in proximity of 300 MPa. A possible estimation could be obtained as the average between the lower stress level leading to failure and the run-out stress level, as indicated by the dashed horizontal lines drawn on Figs. 8a-c. Statistical regression obtained from the data points of the S3 specimens leads to a $\sigma_{max50\%}$ of 277 MPa. Differently, the fatigue limits obtained for the other thicknesses are more conservative (197 and 231 MPa for S1 and S5, respectively). To analyze the data from a different perspective, the plot in Fig. 8d collects all the data points, only with 50% regression line for each series. Due to the significant overlap between the curves, it is possible to claim that the thickness effect is mild on the axial fatigue behavior of the specimens. Indeed, statistical analysis performed on the entire dataset indicates a strong correlation with a scatter index of T_σ=1.46, and an average k= 3.98. In light of this, and considering that the UTS of the material is likewise not dependent on the thickness (Tab. 1), the fatigue data are reported in Fig. 8e in terms of normalized stress (σ_{max}/UTS), with the corresponding statistical analysis. This allows us to draw a generalized conservative result regarding the fatigue limit at 2 million cycles: with a confidence level of 90%, the maximum bearable stress is less than 20% of the UTS.

Comparison between the fatigue data obtained in the present study and other works available in the literature revealed the similarity of the results. In [20], the fatigue endurance in terms of stress amplitude of as-sintered 17-4 PH MEAM specimens tested in uniaxial fatigue with R=0.1 was reported as 146.25 MPa, corresponding to a maximum stress of 325 MPa. In [11], MEAM specimens with solid infill and circular cross-sections tested in uniaxial fatigue with R=0.1 resulted in a fatigue limit below 20% of the UTS, which, in terms of stress amplitude, is reported as 223 MPa. The reduction of the fatigue limit of MEAM specimens is significant in comparison to wrought counterparts. A fatigue limit of 450 MPa expressed in stress amplitude (corresponding to a maximum stress of 1000 MPa) is reported in [11], while in [26] conventionally manufactured 17-4 PH specimens subjected to heat treatments H900 and H1150 were tested under rotating bending fatigue (R=-1) resulting in a fatigue limit of 550 and 525 MPa, respectively (1100 and 1050 MPa in terms of maximum stress). In the latter study, 17-4 PH specimens produced via Binder Jetting were also tested in heat treated conditions, showing a fatigue behavior relatively close to the one reported in the present work and below the performances of the conventional counterparts.

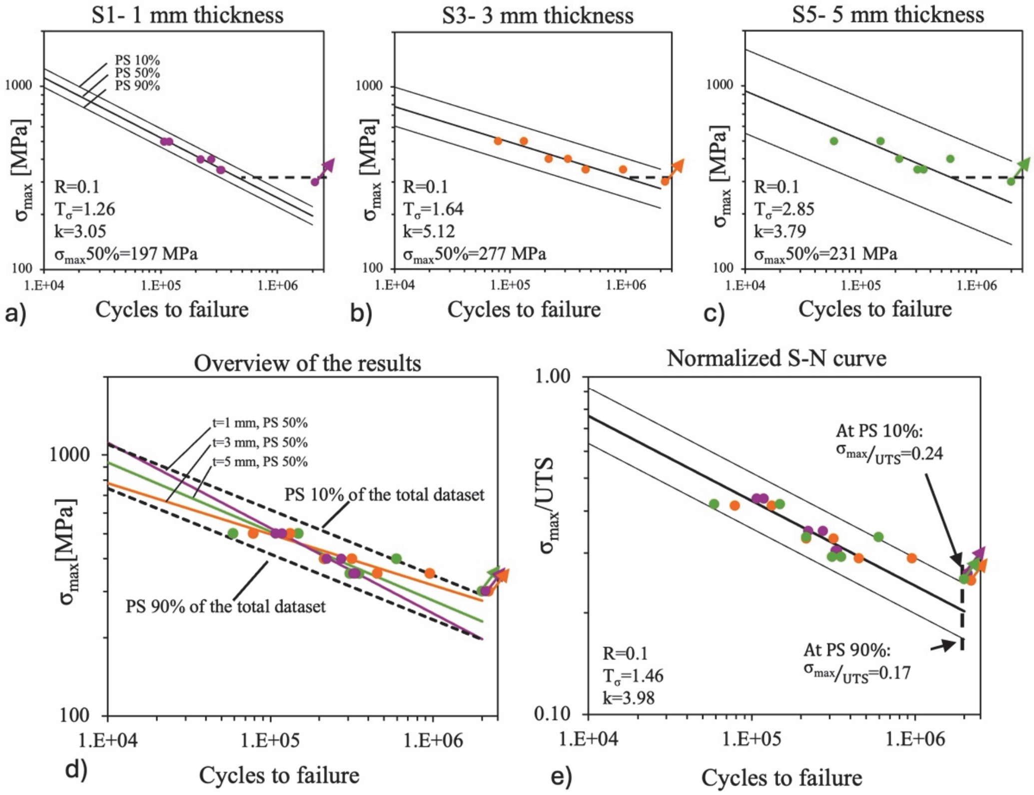

Figure 8: S-N curves expressed in terms of maximum stress amplitude for each thickness, S1 a), S3 b), and S5 c). d) overview of the results proposed as a unique dataset, e) normalized S-N curves over the average UTS of the three series.

Fractography

For a better understanding of the fracture mechanisms, Fig. 9 reports representative fracture surfaces collected with SEM as well as three-dimensional reconstructions of the fracture surfaces obtained with the confocal microscope. It is well known that fatigue is often a superficial phenomenon since asperities and irregularities on the external surfaces are dominantly responsible for stress intensification, and thus crack initiation. However, the internal surfaces of large voids induced by the printing procedure in MEAM might as well act as free surfaces, and crack initiation points can be observed from the inside of the specimens rather than from the outer surface [27]. As it can be inferred from the images reported in Fig. 9, in the present work, the majority of the failures initiated from surface defects. In particular, a very frequent crack initiation point (5 cases observed, which means less than 30% of the total number of failed specimens) was located at one of the bottom corners of the specimens. Those significantly deformed corners presented an acute angle, and thus are believed to act as major stress intensifiers. The deformation was probably caused by different factors: first, the bottom layers must bear the weight of the part during printing, which provokes a relaxation of the bottom parts, a defect usually referred to as elephant foot [28]. Moreover, due to the constant contact with the warm printing platform, the first layers have a more intense thermal history. Thus, the bottom part of a print is generally exposed to high temperatures for longer times, both during the printing and during the sintering process, and this condition favors the deformation.

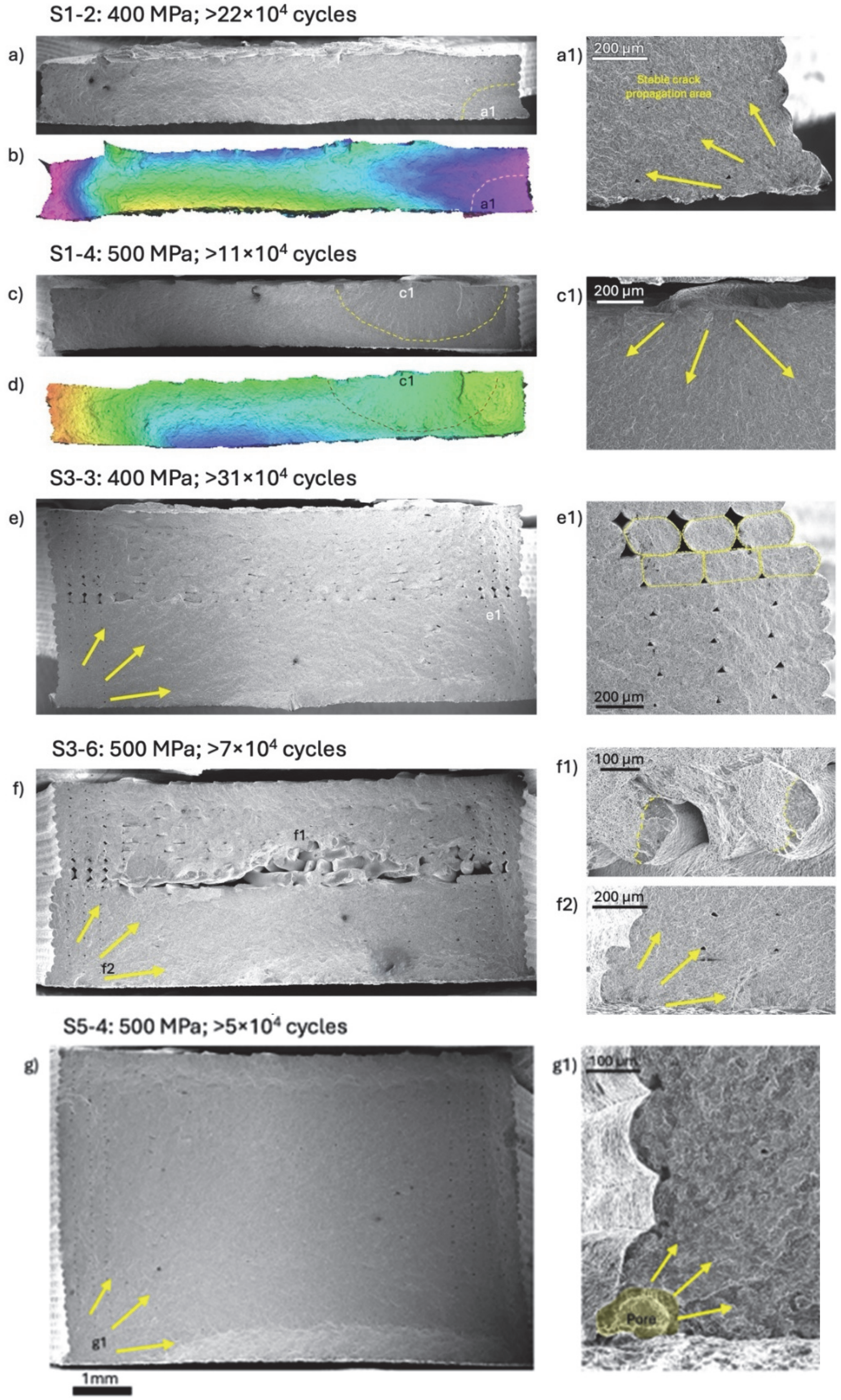

Figure 9: Fractography analysis of the smooth specimens. S1-2: SEM image of the whole fracture surface a) and crack initiation point a1), morphological IFM image b). S1-4: images c), c1), and d), same description as S1-2. Following: SEM images of the whole fracture surfaces and magnifications for S3-3 e), and e1); S3-6 f), f1), and f2); S5-4 g) and g1).

Another frequent crack initiation point (7 cases, which means less than 40% of the failed specimens), was observed on the top surfaces. Here, the printing strategy consisted of overlapping adjacent rasters that created an irregular surface. Similar observations were reported by Suwanpreecha et al. [20], who identified the following typical crack initiation points in as-sintered 17-4 PH MEAM specimens: notches derived from the deposition strategy on the top surface, Al_2O_3 inclusions on the bottom surface, and interlayer notches on the side surfaces. However, the bottom corner initiation point was not reported as a probable failure location. It must be noted that in our specimens, Al_2O_3 inclusions were never identified since no rafts were printed, thus the ceramic was not required.

Figs. 9a-d collect two examples of fracture surfaces of S1 specimens that were chosen to show the two typical crack mechanisms described above. The morphological images obtained with the confocal microscope offered valuable insight, since their distinct features effectively highlighted the different stages of crack propagation with enhanced contrast. In the first specimen, S1-2, the crack initiation point was located on a very deformed bottom corner, while in the second one, S1-4, the initiation occurred at a surface irregularity on the top surface related to the deposition of the top layer. It must be noted that the infill of the specimens was very dense, and the only visible pores were on the sides, marking the four external contour walls. Figs. 9e-f are dedicated to two examples of S3 specimens. As already shown in Fig. 4, the quality of the S3 batch was lower in comparison to the other series, as all of the S3 specimens were affected by a horizontal array of pores in the middle of the thickness, indicating that some accident occurred during the printing phase. In particular, from the detail in Fig. 9e1, it is possible to observe a ‘step’ on the side of the specimen, suggesting a sudden displacement of the relative position of the nozzle and printing platform. Moreover, the cross-sectional shape of the rasters of the external walls switched from elliptical to almost circular. This might be attributed to several factors, such as a decrease in the extrusion temperature, an increase in the extrusion speed, or an increase in the distance between the nozzle and the printing plane. Possibly, some external factors contributed to this issue, such as a vibration of the floor where the machine was placed. However, in specimen S3-3, the voids in the middle section did not provide crack initiation points, and the deformed bottom corner was confirmed as the most dangerous point of the section. Alongside specimen S3-3, the fracture surface of S3-6 was selected because it shows the poorest infill homogeneity observed. A large area in the middle of the cross-section was characterized by an almost complete lack of adhesion between rasters and layers. This specimen might have been the origin of the ‘accident’ that induced the mid-thickness array of pores in all the specimens of the batch. Interestingly, multiple crack initiation points were observed on each raster in the middle area, as shown in Fig. 9f1. However, these cracks were small in comparison to the extension of the fatigue crack growth area that was initiated at the bottom corner depicted in detail in Fig. 9f2. This observation could indicate that internal defects were less determinant in terms of fatigue initiation than external defects.

Fig. 9g shows the typical fracture surface of an S5 specimen, with the initiation point at the bottom corner. The specimen presented, S5-4, is particularly interesting since a wide circular pore with equivalent diameter of 74 µm was located exactly on the most critical corner, which probably resulted in a faster crack initiation. The bar plot presented in Fig. 10 helps to visualize the frequency of the failure locations from the bottom corner and the top surfaces. Note that some specimens presented multiple initiation points in both the abovementioned locations. The category ‘Others’ includes the few specimens that failed from other locations, such as irregularities on the bottom layer. It must be noted that no specific trend was derived correlating the cycles to failure to the crack initiation location.

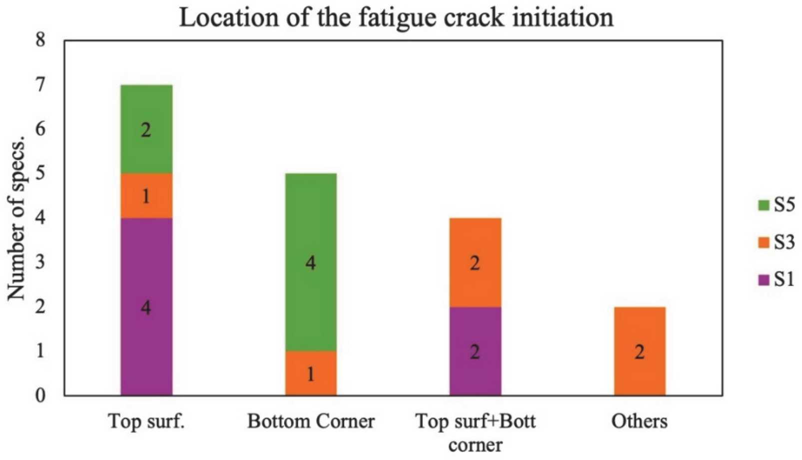

Figure 10: Distribution of the crack initiation sites on the smooth specimens tested.

Notch effect

To complete the investigation of the design effect on the fatigue properties of 17-4 PH specimens, the notched specimens were tested in the same conditions as the smooth specimens. Due to the sintering cracks described in the previous section, the fatigue curves obtained, as well as the parameters calculated as the fatigue notch factor, are to be considered conservative in comparison to what could possibly be obtained from well-formed notches. Nonetheless, for explorative purposes, the S-N curves obtained with the N90 and N30 series are reported here and compared with the S-N curve of the smooth specimens with identical thickness, i.e., S3. Although the S3 batch is entirely affected by extended internal porosity, the previous sections have proven a limited impact of the porosity on the mechanical tests, especially on the fatigue tests, where superficial defects were dominant. In this context, the comparison proposed seems reasonable. The negative inverse slope and scatter index of the notched specimens are similar, as reported in Fig. 11a. Note that some points fall into the low-cycle fatigue area, which is below 10^4 cycles; they were excluded from further analysis.

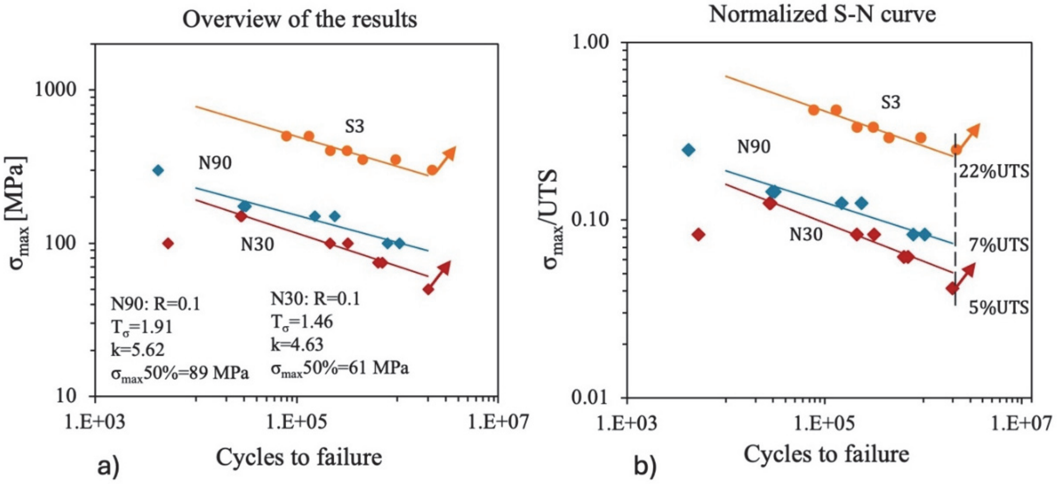

Figure 11: a) comparison of the S-N curves expressed in terms of maximum stress amplitude between the notched and the smooth specimens with identical thickness, S3. b) normalized S-N curve over the average UTS of the material.

In terms of normalized S-N curves, shown in Fig. 11b, the fatigue limit of the notched specimens obtained from the statistical analysis based on the ISO 12107 [25] is below 7% and 5% of the UTS obtained with the smooth S3 specimens, respectively, for the N90 and N30 series. The decrease of the fatigue limit in comparison to the smooth counterparts, represented as the ratio ($\sigma_{max50\%}$smooth)/($\sigma_{max50\%}$notched) is 3.11 and 4.54 for N90 and N30, respectively. These values can be considered as estimations of the notch factor k_f. The calculation of the latter might also be carried out following Peterson's approach, which enables the calculation of the notch sensitivity index q through empirical formulations that can be found in [29] based on the notch radius and the UTS of the material. Although the material under consideration is not homogeneous and presents a surface with enhanced roughness and defects, the approach provides a useful indication on the notch sensitivity of the specimens investigated. The notch sensitivity index is an indicator of how much the notch affects the stress field in the specimen. It ranges from 0 to 1, where 1 corresponds to complete sensitivity to the notch. Once q is obtained, k_f is calculated from the relation $q=(k_f-1)/(k_t-1)$. The stress concentration factor k_t for the investigated notches was obtained from a simple finite element (FE) analysis in the commercial software Abaqus. In the FE model, a known stress (1 MPa) was applied to the notched specimens to compute the maximum stress at the notch apex, the so-called peak stress, and the nominal stress in the notched section, at a sufficient distance from the notch. A 2D model was designed in Abaqus based on the CAD model of the smooth specimen, with symmetrical boundary conditions to consider only one quarter of the geometry. The mesh was obtained with quadratic CPE8R elements and refined towards the notch tip based on a sensitivity analysis to a minimum element size of 0.05 mm. The factor k_t is simply the ratio between the peak stress and the nominal stress. The values of q, k_t, and k_f obtained for each notch geometry are reported in Tab. 2. Note that the k_t calculated for the smooth specimens, for mere comparative purposes, is almost 1, as well as the notch sensitivity index. This confirms that the radius of the rounded sides of the smooth specimens (30 mm) was sufficient to avoid stress intensification. As reported in Tab. 2, the k_f values obtained for the N90 and N30 specimens are respectively 4.14 and 5.03. These values are more conservative than the estimations obtained from the empirical ratio reported above (3.11 and 4.54). The notch sensitivity index depends on the manufacturing process as well. For example, in [30], the index q was measured by testing smooth and notched 17-4 PH specimens produced via a laser powder bed fusion (PBF-LB) technique. The result of the investigation revealed that due to the specimens' extensive porosity and poor surface roughness, the detrimental effect of the notch on the fatigue behavior of the specimens was minor.

Specimen series	Thickness [mm]	$\sigma_{max\ 50\%}$ [MPa]	Max σ_{max} at run-out [MPa]	T_σ	k	ϱ [mm]	k_{tn}	q	k_f
S1	1	197	300	1.26	3.05				
S5	5	231	300	2.85	3.79				
S3	3	277	300	1.64	5.12				
N90	3	89	--	1.91	5.62	0.2	5.17	0.75	4.14
N30	3	61	50	1.46	4.63	0.1	7.67	0.60	5.03

Table 2: Fatigue properties for all tested specimens.

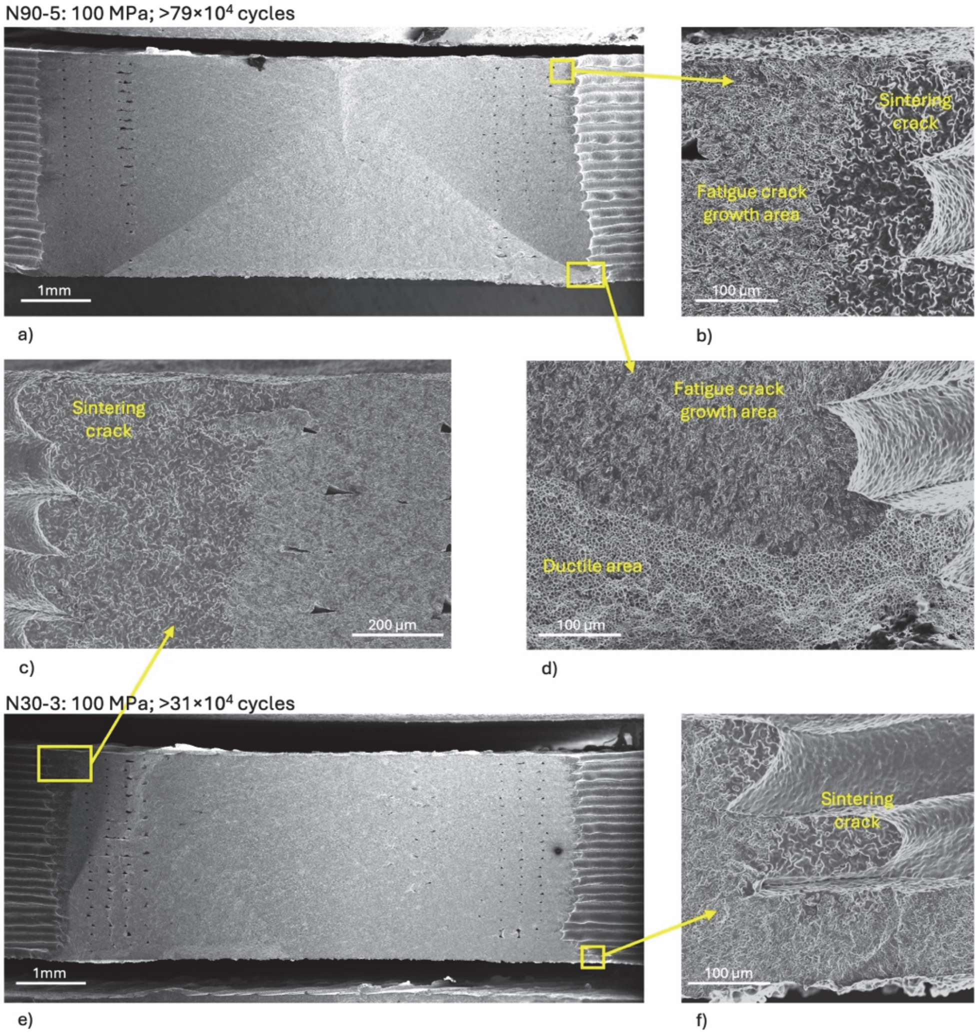

Figure 12: Fractography analysis of the notched specimens. N90-5: SEM image overview of the fracture surface, a), and magnified details in b) and d). N30-3: overview of the fracture surface e), and magnified details s in c) and f).

Fig. 12 reports representative fracture surfaces for both the notched series. Through the magnified details, it is possible to observe the morphology of the surfaces of the sintering cracks that are well-developed from both sides in the N30-3 specimen. On the contrary, in the N90-5 specimen, only a very limited portion of material shows the morphology of the sintering crack as depicted in detail in Fig. 12c. These examples demonstrate that fatigue cracks tend to originate from the sintering crack tips. Otherwise, the fatigue initiation points can be located at the notch root without a preferential location. This suggests that in the presence of notched geometries, irregularities such as deformed corners and rough top surfaces are not as critical as they were proven in the previous section in the case of smooth fatigue specimens.

CONCLUSIONS

The experimental campaigns presented proved the reliability of the Markforged fabrication process of 17-4 PH specimens with different thicknesses and varying geometrical details. However, various fabrication problems affected the specimens' fatigue behavior. The key findings of the research are reported as follows:

1. The commercial MEAM system utilized is more robust compared to commercial FDM printers for the fabrication of similar specimens and enables efficient fabrication of a large number of specimens. Moreover, characteristics such as internal porosity, shrinkage, surface roughness, microhardness, and tensile properties showed high repeatability, consistent with similar studies available in the literature. The density of the infill was remarkable, although vertical arrays of pores were visible between the external walls. However, serious limitations in terms of geometrical details were encountered. The thinnest sections suffered from warping, and small notch radii could not be obtained with precision. In addition, notches with an opening angle of 30° exhibited sintering cracks due to the shrinkage during sintering. A similar effect was observed, though to a lesser extent, with notches featuring opening angles of 90°.
2. With regard to the thickness effect, the specimens considered (with 1, 3, and 5 mm thickness) represented similar mechanical performance. Microhardness was consistent across the specimen cross-sections, with average values of 347±8, 366±8, and 349±8 HV0.2 for the three thicknesses. Due to the absence of a clear microhardness trend with the thickness, the thickness effect is deemed irrelevant to the microhardness measures. Tensile testing indicated that all smooth specimen series exhibited comparable strength, with average yield stress and UTS of 1053±36 MPa and 1185±31 MPa, respectively. Young's modulus was also consistent across specimens, averaging 215.2±5.3 GPa. The elongation to fracture was the only parameter displaying an upward trend with increasing thickness, ranging from 1.6% to 3.2%.
3. Within the limitations of the present experimental campaign, thickness variation did not impact the axial fatigue behavior of the smooth specimens. The statistical fatigue limits calculated at 50% PS were 197, 277, and 231 MPa for the S1, S3, and S5 series, respectively. The data points of the three batches represent a strong correlation and can be represented by narrow scatter bands (T_σ=1.46). Normalization of the S-N curves over the average UTS facilitates comparison. The statistical fatigue limit of the MEAM specimens falls below 20% of the UTS, while it has been reported that wrought 17-4 PH specimens can reach a fatigue limit of 40% of the UTS. Fractographic analysis shed light on the reduced fatigue strength of the MEAM specimens, highlighting how superficial irregularities derived from the printing strategy act as detrimental stress risers and crack initiation points. Most of the tested specimens failed because of irregularities on the top surface, related to the overlap of adjacent rasters. The second most frequent failure site was one of the bottom corners of the specimens, which was highly deformed. Notably, the internal porosity was too scarce to imply critical stress intensification.
4. The statistical fatigue limit of notched specimens was less than 50% of that observed in smooth specimens of equivalent thickness, and further decreased as notch sharpness increased. Fatigue strengths corresponded to 7% and 5% of the UTS, respectively, for the N90 and N30 series. It must be noted that the sintering crack effect and the notch geometry effect could not be separated, and future research is required to properly evaluate the fatigue limit of notched parts. The notch factors determined using Peterson's method (neglecting the sintering cracks) tended to be more conservative than those derived from comparing fatigue results between smooth and notched specimens based on the ratio of their statistical fatigue limits. Fractographic analysis demonstrated that fatigue crack propagation initiated at the apex of sintering cracks, which were frequently observed on both sides of the notched specimens. In the few specimens where no sintering cracks were detected, mostly belonging to the N90 series, the fatigue crack initiation was located at the notch root.

AUTHORS CONTRIBUTIONS

SS: Methodology, Validation, Formal Analysis, Investigation, Data Curation, Writing-Original Draft, Visualization; **AH:** Investigation, Writing-Review & Editing; **OM:** Investigation, Resources; **SB:** Methodology, Validation, Writing-Review & Editing, Supervision; **NR:** Conceptualization, Methodology, Validation, Resources, Writing-Review & Editing, Supervision, Project administration

REFERENCES

[1] Bankapalli, N.K., Gupta, V., Saxena, P., Bajpai, A., Lahoda, C., Polte, J. (2023). Filament fabrication and subsequent additive manufacturing, debinding, and sintering for extrusion-based metal additive manufacturing and their applications: A review, Compos. Part B Eng., 264, p. 110915. DOI: https://doi.org/10.1016/j.compositesb.2023.110915.

[2] Costa, J.M., Sequeiros, E.W., Vieira, M.F. (2023). Fused Filament Fabrication for Metallic Materials: A Brief Review, Materials, 16(24), p. 7505. DOI: https://doi.org/10.3390/ma16247505.

[3] Altıparmak, S.C., Xiao, B. (2021). A market assessment of additive manufacturing potential for the aerospace industry, J. Manuf. Process., 68, pp. 728–738. DOI: https://doi.org/10.1016/j.jmapro.2021.05.072.

[4] Spiller, S., Berto, F., Razavi, N. (2022). Mechanical behavior of Material Extrusion Additive Manufactured components: an overview, Procedia Struct. Integr., 41, pp. 158–174. DOI: https://doi.org/10.1016/j.prostr.2022.05.018.

[5] Metallic and Ceramic Components by the Material Extrusion of Highly-Filled Polymers: A Review and Future Perspectives, Materials, 11(5), p. 840. DOI: https://doi.org/10.3390/ma11050840.

[6] Galati, M., Minetola, P. (2019). Analysis of Density, Roughness, and Accuracy of the Atomic Diffusion Additive Manufacturing (ADAM) Process for Metal Parts, Materials, 12(24), p. 4122. DOI: https://doi.org/10.3390/ma12244122.

[7] Henry, T.C., Morales, M.A., Cole, D.P., Shumeyko, C.M., Riddick, J.C. (2021). Mechanical behavior of 17-4 PH stainless steel processed by atomic diffusion additive manufacturing, Int. J. Adv. Manuf. Technol., 114(7–8), pp. 2103–2114. DOI: https://doi.org/10.1007/s00170-021-06785-1.

[8] Suwanpreecha, C., Seensattayawong, P., Vadhanakovint, V., Manonukul, A. (2021). Influence of Specimen Layout on 17-4PH (AISI 630) Alloys Fabricated by Low-Cost Additive Manufacturing, Metall. Mater. Trans. A, 52(5), pp. 1999–2009. DOI: https://doi.org/10.1007/s11661-021-06211-x.

[9] Alkindi, T., Alyammahi, M., Susantyoko, R.A., Atatreh, S. (2021). The effect of varying specimens' printing angles to the bed surface on the tensile strength of 3D-printed 17-4PH stainless-steels via metal FFF additive manufacturing, MRS Commun., 11(3), pp. 310–316. DOI: https://doi.org/10.1557/s43579-021-00040-0.

[10] Abe, Y., Kurose, T., Santos, M., Kanaya, Y., Ishigami, A., Tanaka, S., Ito, H. (2021). Effect of Layer Directions on Internal Structures and Tensile Properties of 17-4PH Stainless Steel Parts Fabricated by Fused Deposition of Metals, Materials, 14(2), p. 243. DOI: https://doi.org/10.3390/ma14020243.

[11] Lawrence, B.D., Henry, T.C., Phillips, F., Riddick, J., Kudzal, A. (2023). High-cycle tension-tension fatigue performance of additively manufactured 17–4 PH stainless steel, Int. J. Adv. Manuf. Technol., 126(1–2), pp. 777–786. DOI: https://doi.org/10.1007/s00170-023-11146-1.

[12] Rodriguez, J., Zuriarrain, A., Madariaga, A., Arrazola, P.J., Dominguez, E., Fraile, I., Soler, D. (2023). Mechanical Properties and Fatigue Performance of 17-4 PH Stainless Steel Manufactured by Atomic Diffusion Additive Manufacturing Technology, J. Manuf. Mater. Process., 7(5), p. 172. DOI: https://doi.org/10.3390/jmmp7050172.

[13] Naim, M., Chemkhi, M., Kauffmann, J., Alhussein, A. (2024). Taguchi DoE analysis and characterization of 17-4 PH stainless steel parts produced by material extrusion (MEX) process, Adv. Ind. Manuf. Eng., 8, p. 100138. DOI: https://doi.org/10.1016/j.aime.2024.100138.

[14] Gonzalez-Gutierrez, J., Arbeiter, F., Schlauf, T., Kukla, C., Holzer, C. (2019). Tensile properties of sintered 17-4PH stainless steel fabricated by material extrusion additive manufacturing, Mater. Lett., 248, pp. 165–168. DOI: https://doi.org/10.1016/j.matlet.2019.04.024.

[15] Standard Specification for Precipitation-Hardening Stainless and Heat-Resisting Steel Plate, Sheet, and Strip, ASTM A693-24, 2024. (n.d.).

[16] Pellegrini, A., Lavecchia, F., Guerra, M.G., Galantucci, L.M. (2023). Influence of aging treatments on 17–4 PH stainless steel parts realized using material extrusion additive manufacturing technologies, Int. J. Adv. Manuf. Technol., 126(1–2), pp. 163–178. DOI: https://doi.org/10.1007/s00170-023-11136-3.

[17] Local characterization of stainless steel 17-4PH produced by material extrusion additive manufacturing: Influence of the post-treatment, Mater. Sci. Eng. A, 880, p. 145371. DOI: https://doi.org/10.1016/j.msea.2023.145371.

[18] Kedziora, S., Decker, T., Museyibov, E., Morbach, J., Hohmann, S., Huwer, A., Wahl, M. (2022). Strength Properties of 316L and 17-4 PH Stainless Steel Produced with Additive Manufacturing, Materials, 15(18), p. 6278. DOI: https://doi.org/10.3390/ma15186278.

[19] Ghadimi, H., Jirandehi, A.P., Nemati, S., Ding, H., Garbie, A., Raush, J., Zeng, C., Guo, S. (2023). Effects of Printing Layer Orientation on the High-Frequency Bending-Fatigue Life and Tensile Strength of Additively Manufactured 17-4 PH Stainless Steel, Materials, 16(2), p. 469. DOI: https://doi.org/10.3390/ma16020469.

[20] Suwanpreecha, C., Linjee, S., Newyawong, P., Yordsri, V., Songkuea, S., Wutikhun, T., Manonukul, A. (2024). Effects of aging and shot peening on surface quality and fatigue properties of material extrusion additive manufactured 17-4PH stainless steel, Mater. Des., 241, p. 112939. DOI: https://doi.org/10.1016/j.matdes.2024.112939.

[21] Godec, D., Cano, S., Holzer, C., Gonzalez-Gutierrez, J. (2020). Optimization of the 3D Printing Parameters for Tensile Properties of Specimens Produced by Fused Filament Fabrication of 17-4PH Stainless Steel, Materials, 13(3), p. 774. DOI: https://doi.org/10.3390/ma13030774.

[22] Kurose, T., Abe, Y., Santos, M.V.A., Kanaya, Y., Ishigami, A., Tanaka, S., Ito, H. (2020). Influence of the Layer Directions on the Properties of 316L Stainless Steel Parts Fabricated through Fused Deposition of Metals, Materials, 13(11), p. 2493. DOI: https://doi.org/10.3390/ma13112493.

[23] Spiller, S., Kolstad, S.O., Razavi, N. (2022). Fabrication and characterization of 316L stainless steel components printed with material extrusion additive manufacturing, Procedia Struct. Integr., 42, pp. 1239–1248. DOI: https://doi.org/10.1016/j.prostr.2022.12.158.

[24] Razavi, N., Van Hooreweder, B., Berto, F. (2020). Effect of build thickness and geometry on quasi-static and fatigue behavior of Ti-6Al-4V produced by Electron Beam Melting, Addit. Manuf., 36, p. 101426. DOI: https://doi.org/10.1016/j.addma.2020.101426.

[25] Metallic Materials-Fatigue Testing-Statistical planning and analysis of data, Standard ISO 12107:2012. (n.d.).

[26] Radhakrishnan, J., Kumar, P., Gan, S.S., Bryl, A., McKinnell, J., Ramamurty, U. (2023). Fatigue resistance of the binder jet printed 17-4 precipitation hardened martensitic stainless steel, Mater. Sci. Eng. A, 865, p. 144451. DOI: https://doi.org/10.1016/j.msea.2022.144451.

[27] Spiller, S., Olsøybakk Kolstad, S., Razavi, N. (2023). Fatigue behavior of 316L stainless steel fabricated via Material Extrusion Additive Manufacturing, Eng. Fract. Mech., 291, p. 109544. DOI: https://doi.org/10.1016/j.engfracmech.2023.109544.

[28] Hsiang Loh, G., Pei, E., Gonzalez-Gutierrez, J., Monzón, M. (2020). An Overview of Material Extrusion Troubleshooting, Appl. Sci., 10(14), p. 4776. DOI: https://doi.org/10.3390/app10144776.

[29] Dowling, N. E. (2013). Mechanical Behavior of Materials-Engineering Methods for Deformation, Fracture, and Fatigue, Fouth Edition.

[30] Berto, F., Fatemi, A., Shamsaei, N., Nima Razavi. (2020). Fatigue Assessment of 17-4 PH Stainless Steel Notched Specimens Made by Direct Metal Laser Sintering., Structural Integrity of Additive Manufactured Parts, ASTM International100 Barr Harbor Drive, PO Box C700, West Conshohocken, PA 19428-2959, pp. 415–422.

APPENDIX

Test data, f=20Hz, R=0.1			
Specimen	σ_{max} [MPa]	F_{max} [N]	Cycles to failure
S1-1	300	2579.9	Run-out
S1-2	400	3439.8	221 297
S1-3	400	3439.8	273 171
S1-4	500	4299.8	118 305
S1-5	500	4299.8	107 335
S1-6	350	3009.8	332 881
S1-7	350	3009.8	325 133
S3-1	400	9285.6	216 186
S3-2	350	8124.9	452 751
S3-3	400	9285.6	316 882
S3-4	300	6964.2	Run-out
S3-5	500	11607.0	132 351
S3-6	500	11607.0	78 784
S3-7	350	8124.9	953 736

S5-1	400	14897.5	595 789
S5-3	400	14897.5	214 872
S5-4	500	18621.9	58 842
S5-5	500	18621.9	148 587
S5-6	300	11173.1	Run-out
S5-7	350	13035.3	351 436
S5-8	350	13035.3	308 996
N90-1	300	7399.3	4 184
N90-2	150	3699.7	238 641
N90-3	150	3699.7	150 283
N90-4	100	2466.4	1 040 832
N90-5	100	2466.4	793 021
N90-6	175	4316.3	31 336
N90-7	175	4316.3	29 502
N30-1	50	1353.6	Run-out
N30-2	100	2707.2	214 019
N30-3	100	2707.2	317 962
N30-4	150	4060.8	27 826
N30-5	150	4060.8	28 492
N30-6	75	2030.4	701 477
N30-7	75	2030.4	639 580
N30-8	100	2707.2	5 281

Table A1: Fatigue tests data for the tested specimens.